Microstructure distribution in an AA2050 T34 friction stir weld and its evolution during post-welding heat treatment

B. Malard [a,b,c], F. De Geuser [a,b], A. Deschamps [a,b,*]

[a] Univ. Grenoble Alpes, SIMAP, F-38000 Grenoble, France
[b] CNRS, SIMAP, F-38000 Grenoble, France
[c] CIRIMAT, INPT-ENSIACET, 4 Allée Emile Monso 31030, Toulouse, France

A B S T R A C T

This paper presents a systematic study where the distribution of precipitate microstructures is mapped in the cross-section of a friction stir weld made with an AA2050 Al–Cu–Li alloy in the naturally aged temper, as well as the evolution of this microstructure during subsequent post-welding heat treatment (PWHT). This study is carried out using spatially resolved small-angle X-ray scattering, supported by transmission electron microscopy, differential scanning calorimetry and microhardness mapping. The as-welded microstructure is dominated by solute clusters, while very little precipitation has taken place during the welding operation. During PWHT, the precipitation kinetics in the different zones of the weld is mainly controlled by the local dislocation density inherited from welding, and by the amount of solute available for precipitation, which depends on the volume fraction of welding-induced intermetallics. Pre-deforming the weld before the PWHT results in a very effective strength recovery and a nearly homogeneous distribution of hardness.

Keywords:
Al–Cu–Li alloy
Friction stir welding
Precipitation
Small-angle X-ray scattering

1. Introduction

Friction stir welding (FSW) is now a weld-established technique for solid-state joining precipitation-hardening alloys. The different aspects of tool design, welding process, microstructure and properties have been extensively reviewed [1–3]. Despite remaining in the solid state, obtaining a homogeneous precipitate microstructure across an FSW joint proves to be extremely difficult, because of the combination of temperature excursion and strain, followed by cooling at finite rate, experienced during the welding operation. These thermo-mechanical conditions usually result in a minimum of mechanical properties either in the heat-affected zone (HAZ) or in the thermo-mechanically affected zone (TMAZ), where the temperature reached during welding is in the range of fastest precipitation kinetics [4–6]. This distribution of precipitate microstructures controls the strength and plastic behavior of the joints, fatigue behavior, toughness, and can have important consequences on its corrosion behavior. Optimizing the combination of initial alloy temper, welding conditions and post-welding heat treatment has been attempted. For the last issue, post-welding heat treatments have been observed to generally further enhance the heterogeneity of mechanical properties and microstructures, and therefore bring little added value to the process [6,7]. On some alloy series, such as the 6000 Al–Mg–Si based alloys, the level of understanding has allowed to build a complete chain of models relating the processing parameters to the microstructure, strength and ductility of the weld assembly [7].

In the last 10 years, new generation Al–Cu–Li based alloys have rapidly developed in the context of a fierce material competition in the aerospace sector [8]. Alloys with Li and Cu concentrations of approximately 1 and 3 wt% respectively, such as AA2198 [9] and AA2050 [10], show remarkable combinations of density, modulus, strength, toughness and corrosion resistance. The predominant precipitation of the T_1 phase in T8 ageing condition, which has been shown to have a distinct interaction mechanism with dislocations [11], is thought to be the main parameter for achieving these properties [12], although the microstructure of these alloys can be much more complex. Indeed, a large variety of precipitates can be observed in these alloys [13–17], from the Al–Li binary system (δ' phase), from the binary Al–Cu system (GP zones, θ'' and θ' phases), form the Al–Cu–Mg system for Mg-containing alloys (GPB zones, S′/S phases) and other phases from the Al–Cu–Li system (T_2, T_B). Joining Al–Cu–Li alloys by friction stir welding has received some attention, both from the viewpoint of the resulting microstructure [18–28], mechanical properties [29–33] and corrosion behavior [34–36]. Most microstructure studies have concentrated on alloys

* Corresponding author at: Univ. Grenoble Alpes, SIMAP, F-38000 Grenoble, France.
E-mail address: alexis.deschamps@grenoble-inp.fr (A. Deschamps).

http://dx.doi.org/10.1016/j.actamat.2015.08.068

welded in the T8 temper, whose precipitate microstructure mainly consists of very thin platelets of T_1 particles and some θ' as well as GP zones [9]. Depending on the welding conditions, the precipitate microstructure in the weld nugget has been shown to either consist of a population of T_1, θ' and T_B particles [18,19], or of a full solid solution [21–23]. Intermediate zones (TMAZ, HAZ) consist of partially dissolved, coarsened T_1 precipitates, whose distribution have been mapped in the weld cross-section by spatially-resolved small-angle X-ray scattering (SAXS) [23,26]. Very little work has been devoted so far to Al–Cu–Li welds performed in the T3 state, although they show a very homogeneous hardness distribution [33]. Post-welding heat treatment has been shown to provide some interesting potential after welding in this condition although until now it has not been possible to avoid some remaining heterogeneity within the welded material [27].

This paper aims at describing in detail the microstructure distribution in the cross-section of a 2050T34 weld, and to study how this microstructure evolves during post-welding heat treatments. More precisely, the aim is to understand the controlling parameters that explain the different levels of microstructure heterogeneity that develop during welding and during the post-welding heat treatments. For this purpose, we have performed systematic microstructure mapping by SAXS, which has been shown to be particularly powerful to obtain a complete view of the microstructure distribution in friction stir welds [4,6,23,26,37]. These microstructure maps have been compared to similar maps of microhardness, and complemented by transmission electron microscopy (TEM) and differential scanning calorimetry (DSC).

2. Material and experimental methods

The material studied in the present work is an aluminum–copper–lithium AA 2050 alloy (Al base, 3.5 wt% Cu, 1 wt% Li) provided by Constellium (France). The material consisted of 20-mm thick rolled plates of the T34 metallurgical state, which were solution treated, stretched by 3.5% and naturally aged. The direction of welding was parallel to the rolling (longitudinal) direction of the plates. In this work, plates of 15 mm thickness (obtained from the 20 mm sheets) were friction stir welded with a rotational speed of 400 rpm and a welding speed of 200 mm/min under a load control of 40 kN. A threaded conical pin with a three flat tool was used. The shoulder was smooth and concave with a tilt angle of 1°. Fig. 1 shows optical micrographs of the main zones of the weld (base material BM, heat-affected zone HAZ, Thermo-mechanically affected zone TMAZ and weld nugget). Classically, the nugget has an inverse conical shape, and the transition between the nugget and the TMAZ is much more pronounced in the advancing as compared to the retreating side. In the following, in all profiles or maps, the advancing side will be on the left and the retreating side on the right.

Subsequent to the weld of the T34 material (which will be called hereafter the T3W state) the material was subjected to a heat treatment of 30 h at 155 °C, resulting in what will be called hereafter the T3WT8 state. When studying the ageing kinetics, some T3W samples were also subjected to other ageing times at this temperature of 155 °C from 0 h to 1000 h. Some results are finally compared to a weld realized with the same parameters, on a 2050T8 material, thus heat treated before welding. This last weld, called T8W, is described in detail in a previously published paper [26].

Several experimental techniques such as microhardness and X-ray measurements, described in detail in the next paragraphs, were performed as line-scans across the weld, in the weld cross-section (i.e. in the plane normal to the welding direction). These line scans were performed at three different depths within the welded plate: 1.5 mm from the top surface, in the middle of the plate, and 2 mm from the bottom surface; these locations will hereafter be named respectively the top, middle and bottom lines.

Microhardness was measured using a fully automated Wilson hardness Tukon 1102 apparatus, with a load of 500 g and a dwell time of 10 s. When performing 2D-maps, points were acquired on a grid of spacing 700 μm in the horizontal and vertical directions, on a total width of 60 mm (30 mm on each side of the weld center) and on a height of 12 mm.

Small-Angle X-ray Scattering experiments were performed on the BM02-D2AM beamline of the European Synchrotron Radiation Facility (ESRF). A photon energy of 16.12 keV was used, and the corresponding sample thickness was in the range 500–600 μm. The beam diameter was of the order of 100 μm so that the probed volume for each SAXS measurement was of the order of 10^{-3} mm^3. The SAXS signal was recorded by a CCD camera positioned at 60 then 200 cm from the sample, resulting in a collection range of scattering vectors $q = 4\pi\sin\theta/\lambda$ (where θ is half of the scattering angle and λ is the photon wavelength) of [0.007–0.5 $Å^{-1}$].

The SAXS patterns were interpreted following the same procedure as in [26]. Since the expected phases are either plate-like (essentially T_1, GP-zones, θ') or spheroidal (solute clusters), the signal has been interpreted as the sum of the contribution of spherical precipitates (of radii <10 Å) and flat cylinder particles. Because the diameter of the platelets particles is too large, it cannot be accessed by the SAXS setup used in this study, so that only the thickness and volume fraction will be extracted [26]. To account for the

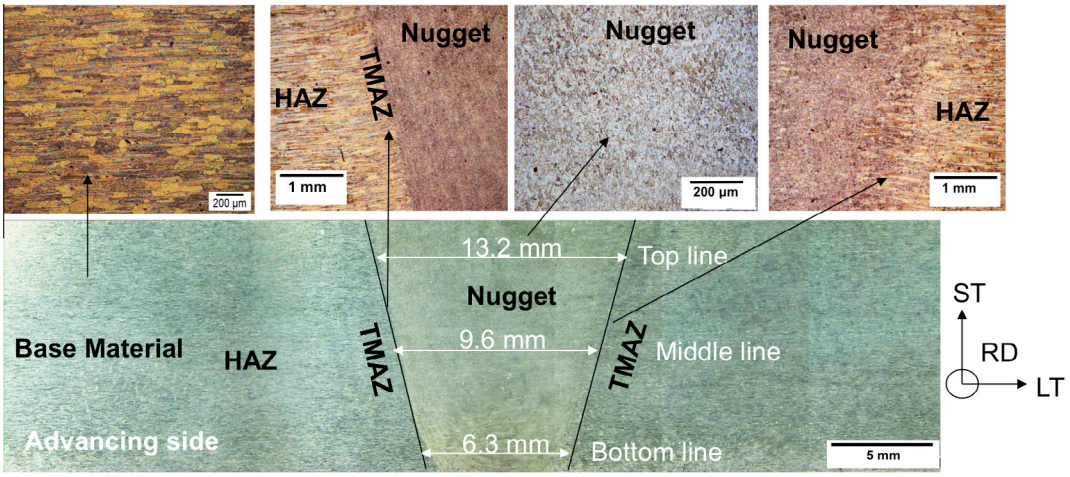

Fig. 1. Optical micrographs showing the shape of the weld nugget in the T34 weld, and the grain microstructure in the different regions of the weld.

contribution of large dispersoids and intermetallics, a further q^{-4} Porod contribution has also be taken into account. Fig. 2a shows the SAXS signal for 3 representative cases (selected from the many thousands SAXS patterns collected during this study) together with the fitted intensity. The blue curve shows a case where only clusters exist (along with the Porod contribution of the large intermetallic and dispersoids). The red curve shows a case where only platelets are present, with a distinct q^{-2} behavior at low q, signature of flat particles [38]. The green case is an intermediate case where both contributions are present.

On a few selected states, transmission electron microscopy (TEM) observations were realized to obtain a direct view of the precipitate microstructure. The samples for TEM observation were first mechanically polished into thin foils of ~100 µm and then electro-polished using a twin double jet system in a solution of 33% nitric acid in methanol at −20 °C and 15 V. Observations were carried out in conventional mode in a JEOL 3010 instrument operating at an accelerating voltage of 300 kV.

Differential scanning calorimetry (DSC) experiments were also carried out on samples collected at different locations in the weld. Samples of thickness ~500 µm and of weight ~50 mg were cut every 3 mm, 40 mm of each side of the weld center at mid-thickness of the sheet. They were subjected to ramp heating between −40 °C and 550 °C at 50 K/min in a TA Q200 apparatus. Results were corrected for baseline and normalized for the sample weight.

Scanning Electron Microscopy observations were realized at an accelerating voltage of 20 kV on a Zeiss Ultra 55 apparatus equipped with an in-lens back-scattered electron detector.

3. Hardness profiles in the different states

Fig. 3 shows hardness profiles in the middle line, realized across the welds in three different states: T3W, T8W, and T3WT8. A number of features can already be observed in these simple profiles, which delineate the main phenomena that will be investigated in the next sections:

- The T3W weld shows a hardness variation between 110 HV and 120 HV, slightly higher than the more consistent 110 HV hardness of the base material. The origin of these variations needs to be understood.
- The T8W weld was described in detail in [26]. In the base metal the material's hardness is 170 HV, and it drops to that of the T3W material in the nugget, due to a full dissolution of the precipitates present before welding and their replacement by solute clusters, which have a smaller hardening efficiency.

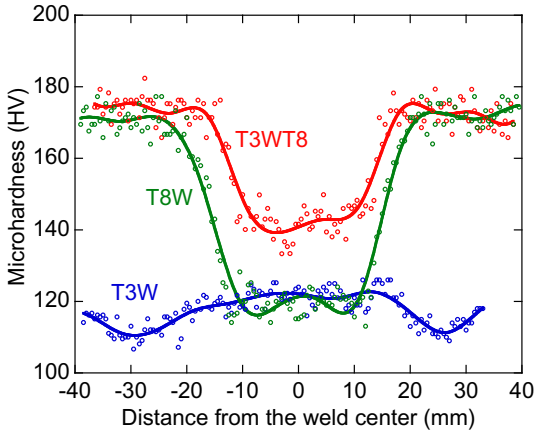

Fig. 3. Hardness profiles in the middle line for the as-welded plate (T3W), after the T8 post-welding heat treatment (T3WT8), compared to a weld realized in the T8 temper (T8W).

- The T3WT8 weld shows a hardness distribution similar to that of the T8W weld far from the weld line, showing as expected that there is no effect of welding on the base material. In the weld center, however, the hardness is higher than that of the T3W state, but still much lower than that of the T8 material, showing that the full strength has not been recovered in the weld nugget. The spatial extension of this hardness drop is also different in the T3WT8 and in the T8W.

The subsequent sections will be devoted to understand in detail the origin of these hardness distributions. In addition, the 2-dimensional distribution of microstructure and hardness will be evaluated in the weld cross-section, as FSW intrinsically induces differences as a function of the distance from the top shoulder (see e.g. [37]).

4. Microstructure distribution and related hardness distribution in the as-welded condition

In the T3W state, TEM observations made in various locations of the weld joint (HAZ, TMAZ and nugget) did not show the presence of hardening precipitates. This is confirmed, in the nugget, by the selected area diffraction pattern shown in Fig. 6f, which is exempt of precipitate diffraction spots and shows only in addition to the matrix spots some diffuse streaks that are probably due to the

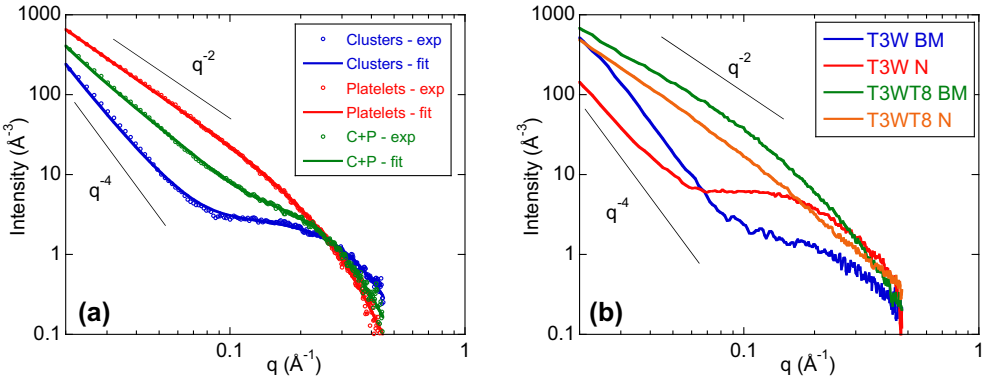

Fig. 2. (a) Comparison between the experimental SAXS intensity and the fitted profile in three representative cases containing respectively a majority of clusters, of platelets, and combining these two types of objects (C + P). (b) Representative SAXS profiles of the T34 base material (T3W BM), of the T3W nugget (T3W N), of the T8 base material (T3WT8 BM) and of the T3WT8 nugget (T3WT8 N) ;

presence of GP zones. A more statistical view of the microstructure, however, requires more appropriate tools. Therefore, three microstructure profiles were realized in the top, middle and bottom lines by spatially-resolved SAXS (measurements separated by 500 μm).

Radially averaged SAXS profiles, representative of the base metal and the weld nugget are shown in Fig. 2b as blue and red lines, respectively. At small scattering vectors, the q^{-4} scattering behavior is due to the presence of the intermetallics and dispersoids. In this range of scattering vectors and in the absence of hardening precipitates, there also can be a small contribution of the dislocation density, however with a smaller power law exponent (of the order of −3) [39,40]. This scattering contribution is observed to decrease from the base metal to the nugget material. This decrease can be due to a change in the distribution of intermetallics (size and/or volume fraction) as well as to a decrease of dislocation density. At large scattering angles, the shoulder is typical of very small solute clusters [9], which have formed during natural ageing in the T34 state and after welding in the nugget zone. Interestingly, the cluster distribution appears to be quite different in the two materials. This point will be quantified more systematically on the SAXS line profiles.

A selection of SAXS images is shown along the middle line of the weld in Fig. 4a. These images reveal mostly isotropic patterns extending to large scattering vectors, characteristic of the very small solute clusters, similarly to that observed in the weld nugget of the T8W weld [26]. In the TMAZ, a small contribution of streaks arises on these patterns, revealing a limited amount of precipitation of platelet precipitates. The HAZ shows visually a smaller amount of clusters as compared to the base material.

The SAXS images give access to the radius and volume fraction of these clusters (for the latter in arbitrary units, because their chemical composition is unknown). These results are plotted in Fig. 4b along with the microhardness profiles, realized in the same locations. It appears that the weld nugget shows a well-defined maximum in cluster size, while the TMAZ shows a maximum of cluster volume fraction and the HAZ a minimum. Altogether, the distribution of hardness appears to be well correlated with the cluster radius. A more complete view of the hardness distribution in the full weld cross-section is shown in Fig. 5a. Consistently with what is observed in the profiles, the hardness is higher on average in the nugget and TMAZ, and the zone of higher hardness follows the shape of these zones, with a larger extension at the top compared to the bottom.

As a summary, the precipitate microstructure after welding consists of a complex spatial distribution of solute clusters. However, only the TMAZ shows some indication of a small amount of higher temperature phases, such as T_1 precipitates. Elsewhere, no such phases are detected, presumably due to a very short time spent at high temperature during the welding operation.

5. Microstructure distribution and related hardness distribution after post-welding heat treatment

As shown in Fig. 3, the SAXS profiles of the base metal subjected to a T8 heat treatment (T3WT8 BM) and of the nugget of the same weld (T3WT8N) both show a q^{-2} behavior, indicating the presence of platelet precipitates. However, the signal is lower in the nugget.

Fig. 6 shows TEM micrographs and associated selected area diffraction patterns for these two conditions. In the $\langle 1\,1\,0\rangle_{Al}$ zone axis, two out of the four variants of the T_1 platelets lying on the $\{1\,1\,1\}_{Al}$ matrix planes, are imaged edge-on and give rise in the selected area diffraction pattern to streaks normal to the precipitate habit plane. One out of the three θ′ platelets lying on the $\{1\,0\,0\}_{Al}$ matrix planes is also imaged edge-on in this zone axis. In the $\langle 1\,0\,0\rangle_{Al}$ zone axis, two out of the three θ′ platelets are imaged edge on, normal to each other.

These observations evidence a very different microstructure in the two regions. The microstructure of the base material is dominated by the presence of T_1 precipitates in the form of very thin platelets, as expected in such an alloy, stretched before ageing and subsequently heat treated at 155 °C [41]. The average diameter of the T_1 platelets in the base metal as measured on TEM images is 54 ± 12 nm. This domination of the precipitate microstructure by T_1 precipitates is confirmed by the selected area diffraction (SAD)

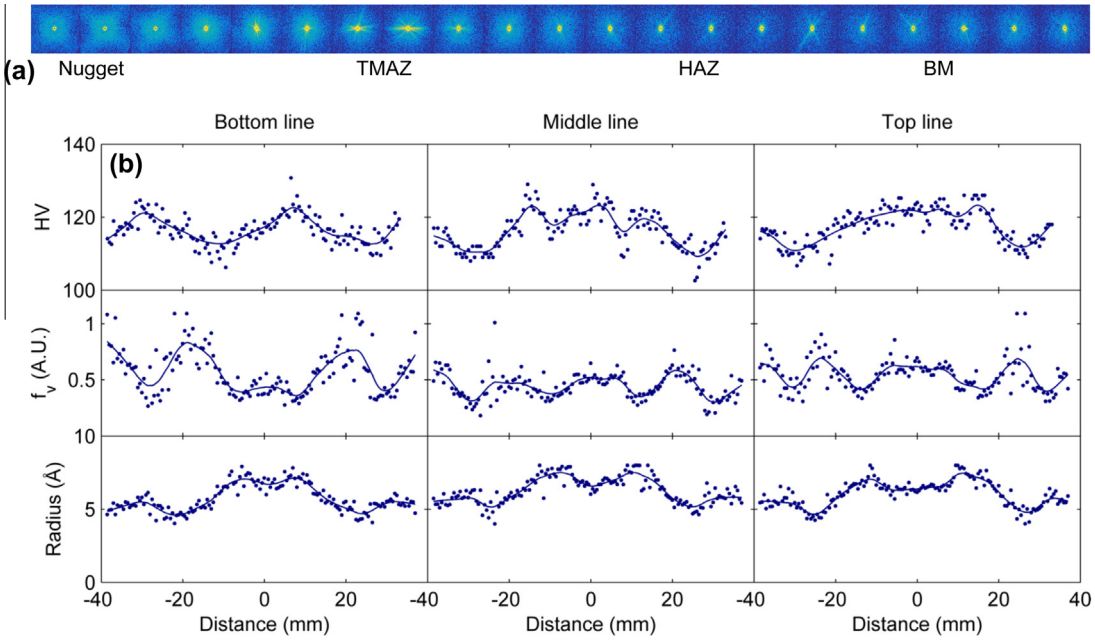

Fig. 4. (a) Series of SAXS images on the retreating side of the T3W weld ranging from the nugget to the base material; (b) Profiles of hardness, cluster volume fraction and cluster radius measured along the three characteristic lines in the T3W weld.

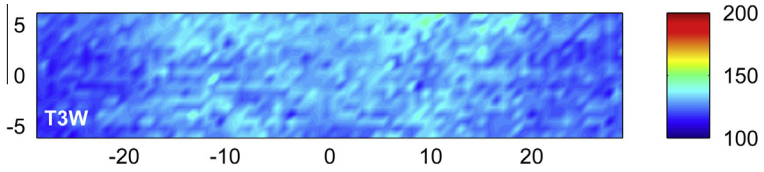

Fig. 5. Hardness map of the T3W weld cross-sections. Color scale is in HV and map scale is in mm.

in the ⟨1 1 0⟩ axis of the matrix (Fig. 6c) showing intense diffraction spots and streaks corresponding to the different T_1 variants. In contrast, the microstructure in the weld nugget shows fewer T_1 precipitates, as confirmed by the fainter diffraction spots and streaks on the SAD pattern (Fig. 6d), and contains mostly θ′ particles on $\{1\,0\,0\}_{Al}$ planes, as confirmed by the strong diffraction spots and streaks in the ⟨1 0 0⟩ matrix zone axis (Fig. 6e). These θ′ particles have a diameter of 51 ± 9 nm, whereas the few T_1 particles observed have a diameter of 126 ± 26 nm.

The complete distribution of these platelet precipitates in the weld cross-section was mapped using SAXS. Similarly to Fig. 4a for the T3W weld, Fig. 7a shows a series of SAXS images from the nugget zone to the base metal of the T3WT8 weld. All the images show a signal dominated by streaks, representative of the presence of platelet precipitates in a textured polycrystal with a relatively large grain size (where the streaks from precipitates do not average to an isotropic signal) [26,42]. From these patterns the behavior appears to be quite uniform in the base material and HAZ (which therefore cannot be defined) and a lower, more diffuse signal is observed in the nugget and TMAZ. It should be noted that the SAXS measurements cannot distinguish between T_1 and θ′ platelets, which have different compositions and habit planes. Because of the unknown sampled texture and mixture of different phases, the volume fraction deduced from SAXS cannot be known on an absolute scale and will be given in arbitrary units.

The full microstructure map, obtained from the analysis of the 3000 SAXS measurements acquired by scanning the weld cross-section with a step of 500 μm, is shown in Fig. 7b and c, in terms of platelet thickness and volume fraction. The first striking feature, consistent with the first observation made in Fig. 3, is the small volume fraction present in the nugget zone. This small volume fraction delineates the nugget and part of the TMAZ, and does not extend much into the HAZ, in contrast to the zone with higher volume fraction of clusters observed in the T3W state. Therefore, precipitation during the T8 post-welding treatment appears to be more limited in the nugget and part of the TMAZ as compared to the rest of the sample, and fairly uniform elsewhere. In terms of precipitate thickness, the platelets appear to be extremely thin (thickness of the order of 1.2 nm) in every location. However, the thickness seems slightly larger in the TMAZ.

This distribution of precipitate microstructures can be related to the distribution of microhardness, which was also mapped across the weld cross-section and is shown in Fig. 5b. In the base metal, the hardness is uniform around 170 HV (T8 hardness). The hardness decreases strongly in the weld nugget, however it is observed to be dependent on the height within this nugget, with the lowest hardness at the bottom of the nugget, and the highest at the top. Moreover, the transition between the base metal and the weld nugget appears to be smoother in terms of hardness than observed on the volume fraction. Actually, in the region of lower hardness but volume fraction similar to that of the base metal, one can observe a higher average platelet thickness (1.5 nm *vs.* 1.2 nm). An increase of the average thickness of T_1 precipitates has actually be shown to be the main parameter explaining the

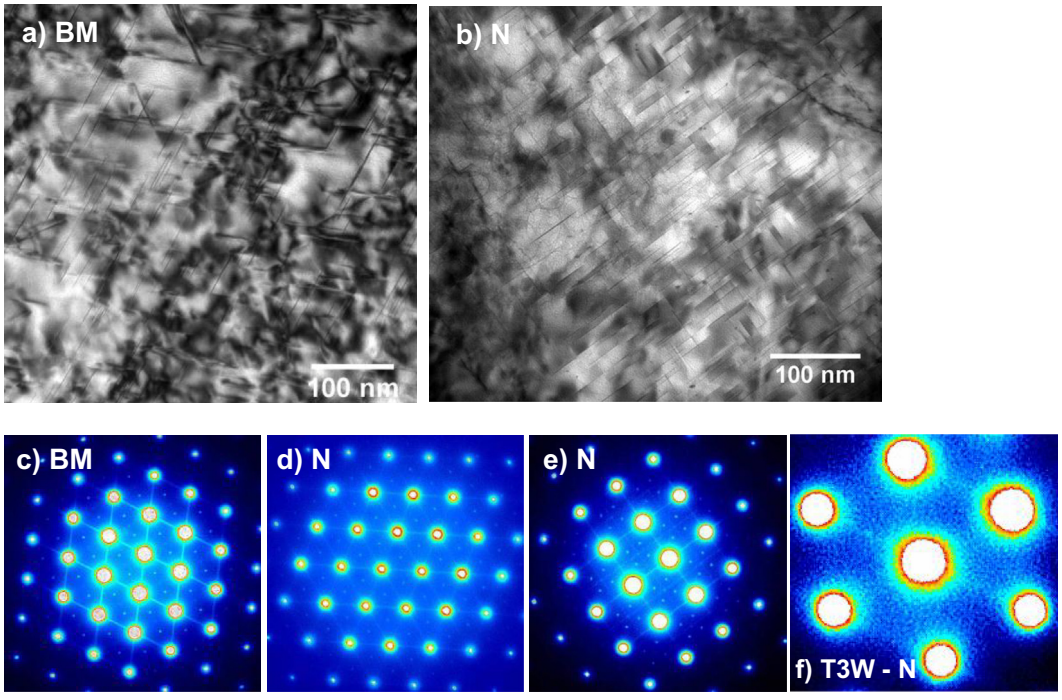

Fig. 6. (a) and (b) TEM bright field micrographs in the base metal (BM) close to $\langle 1\,1\,0\rangle_{Al}$ and in the nugget (N) close to $\langle 1\,0\,0\rangle_{Al}$ in the T3WT8 state; (c) and (d) $\langle 1\,1\,0\rangle_{Al}$ selected area diffraction patterns in the BM and N; (e) $\langle 1\,0\,0\rangle_{Al}$ selected area diffraction patterns in the N; (f) for comparison, $\langle 1\,1\,0\rangle_{Al}$ selected area diffraction pattern of the weld nugget in the T3W state.

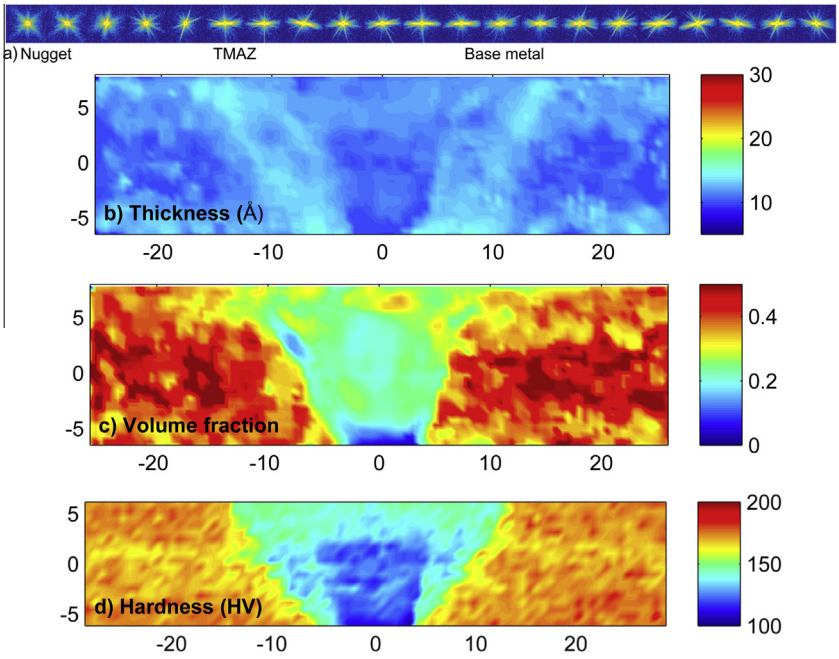

Fig. 7. (a) Series of SAXS images on the retreating side of the T3WT8 weld ranging from the nugget to the base material; (b) and (c) microstructure maps in the T3WT8 cross-section, obtained by analyzing the SAXS images recorded on a grid of 500 μm spacing. (d) Microhardness map of the same weld. Map scale is in mm.

decrease of yield strength during over-aging of Al–Cu–Li alloy [41].

6. Kinetics of microstructure and hardness evolution during the post-welding heat treatment

The previous section has shown that the different zones of the T3W weld, subjected to a T8 post-welding heat treatment, respond differently in terms of precipitation kinetics and strengthening. Major differences are observed in the weld nugget as compared to the base material, and within the weld nugget depending on the depth position in the plate. These differences in behavior were further investigated by performing SAXS and hardness line-scans for the three characteristic heights in the weld (top, middle and bottom) and for a set of different ageing times, some shorter than the T8 heat treatment, and some longer, in order to obtain a full view of the precipitation kinetics in the different zones. The analyzed data is shown in Fig. 8 in terms of the evolution of hardness, precipitate volume fraction and platelet thickness. In these graphs the volume fraction measurements are highly scattered. This dispersion is inherently due to the influence of the local crystallographic texture in the region probed by each SAXS measurements, which acts on the orientation of the platelet precipitates with respect to the X-ray beam, and thus on the scattered intensity.

All the different depths show common features in term of their behavior during heat treatment. The hardness is first observed to drop as soon as the ageing temperature has been reached. As discussed by [9], this is characteristic of the dissolution of the solute clusters formed during natural ageing. Subsequently, after 2 h at 155 °C, the hardness is observed to increase suddenly in the base material, and correspondingly a similar increase in volume fraction is detected. This increase can be attributed to the nucleation and growth of the T_1 precipitates. The time for the formation of these precipitates in a pre-deformed microstructure is comparable with formerly published data in similar conditions [9,41]. The weld nugget appears to follow a very different evolution, since in all locations it remains at a low hardness together with a low volume fraction for these characteristic times. After the T8 treatment of 30 h at 155 °C, the hardness of the base material has stabilized to its plateau value of 170 HV, and is not observed to evolve significantly after. The volume fraction is stable as well. In the weld nugget, however, only at such long ageing times does one observe a hardness and volume fraction increase, which is far from finished at 30 h of ageing. When ageing is pushed to 100 h, the hardness and volume fraction stabilize in the nugget as well. One additional feature that is shared between all three locations is the distribution of platelet thicknesses. Irrespective of ageing time and location in the weld, the thickness is always comprised between 1 nm and 1.5 nm. In terms of T_1 precipitates, this means that the microstructure is in all conditions dominated by single unit cell particles.

The three positions, however, show some differences. A first obvious difference is geometrical in nature: since the width of the weld nugget is higher at the top as compared to the bottom, so is the width of the dip in hardness and volume fraction. A more interesting feature is the behavior at long ageing times (namely the delayed hardening effect in the weld nugget). In the top line, the material reaches a hardness value almost as high as that of the base material, even though it is obtained for much longer ageing times. In the bottom line, however, the hardness remains much lower, reaching a peak value of only 140 HV. This difference is found also in terms of precipitate volume fraction.

This difference of precipitation and hardening kinetics is summarized in Fig. 9, which represents the average hardness evolution in the three regions of the weld nugget compared to that of the base material during ageing. In all locations of the weld nugget, the kinetics of hardness increase is much slower than that of the base material (incubation time 5–10 times longer). The influence of the height appears to be most prominent on the end hardness (which is lower towards the bottom) and not significant on the kinetics (since the time to peak-hardness is similar for the 3 nugget curves).

7. Discussion

Most precipitation hardening Al alloys, when subjected to friction stir welding in the naturally aged condition (T3, T34, or T351 temper) undergo extensive precipitation [3], as it has been

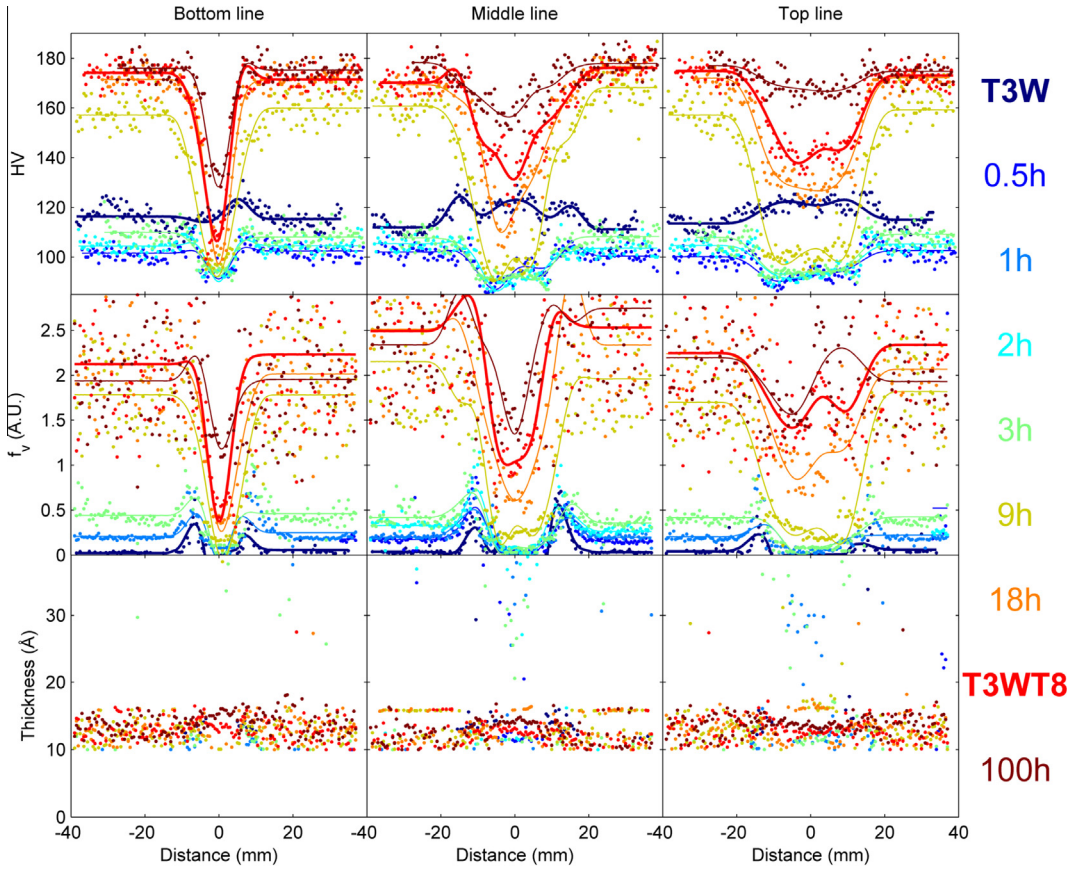

Fig. 8. Results of the line scans of hardness and SAXS measurements in the T3W samples aged for various times at 155 °C, for the three positions in the weld (top, middle and bottom). The T3WT8 sample corresponds to 30 h of ageing.

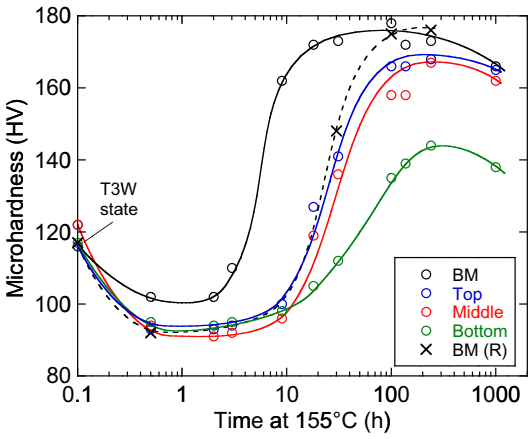

Fig. 9. Summary of hardness evolution during ageing at 155 °C in the base material, for the three locations in the weld nugget and for the re-solutionized base metal – BM(R), see Section 7.

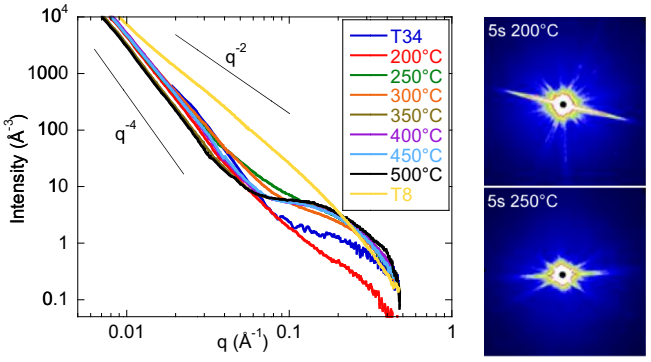

Fig. 10. SAXS profiles of the T34 material, the T8 material, and of the samples subjected to 5 s heat treatments in a salt bath at different temperatures between 200 °C and 500 °C. The SAXS images are shown for 200 °C and 250 °C.

observed in Al–Cu–Mg [4], Al–Mg–Si [5,7], Al–Zn–Mg–Cu [6,37]. Thus, the fact that the T3W weld does not contain a significant fraction of precipitates, but only some solute clusters resulting from post-welding natural ageing, appears to be quite specific to this alloy series. As it is known that the nucleation of T_1 precipitates, which is the main strengthening phase in this alloy, requires some specific features such as the dissociation of a perfect dislocation into partials [43], the absence of precipitates after the welding operation is certainly due to insufficient time spent at high temperature for their formation. To validate this interpretation, a series of T34 samples were subjected to a short ageing time (5 s) at different temperatures from 200 °C to 500 °C in a salt bath, to evaluate the role of a thermal treatment of short duration on the microstructure evolution. A 5 s duration is actually larger than the actual time spent at the peak temperature during a FSW process [7]. Subsequently, these samples were measured using SAXS, after some natural ageing time at room temperature allowing for cluster formation. The results are shown in Fig. 10, along with the SAXS signal corresponding to the initial T34 state and that of the T8 material. As already discussed in Section 4, the T8 material shows at small scattering vectors a behavior close to q^{-2}, which is

characteristic of the presence of a large volume fraction of thin platelets [26,44]. The other materials show at small scattering vectors a behavior close to q^{-4}, which originates from the intermetallics and dispersoids present in the material. In addition, the shoulder at large scattering vectors indicates the presence of solute clusters. The 200 °C sample shows very little, if any, sign of such clusters, confirming (as seen during the first stages of the artificial ageing of the T3W material) that in the range 150–200 °C the solute clusters initially present dissolve. Interestingly, these clusters do not precipitate again after the salt bath heat treatment, whereas they do when the ageing treatment is performed at 250 °C or above. The most likely explanation for this peculiar behavior is a difference in vacancy concentration at the end of these salt bath treatments: at 250 °C and above, the temperature is high enough to induce a renewed supersaturated vacancy concentration, which helps forming a new distribution of solute clusters. This lack of cluster formation is consistent with the HAZ images of Fig. 4a and explains the minimum of volume fraction of clusters observed in the hardness profiles of the T3W weld (Fig. 4b).

No matter the temperature used for the salt bath heat treatment, the SAXS signal does not show the q^{-2} signature of platelet precipitates (as compared to the T8 material), which confirms that very few precipitates form in such a short time at the investigated temperatures. Only at 250 °C and 300 °C, a small but significant signal is detected in the intermediate scattering range (around 0.05 $Å^{-1}$) showing a limited precipitate formation. This signal is confirmed by the presence of streaks on the SAXS images, which are similar to those observed in the TMAZ of the T3W weld (Fig. 4a). Such streaks were not observed at the other ageing temperatures. This temperature range can therefore be expected to the most critical (nose of C-curve) for precipitation in this alloy.

This absence of welding-induced coarse precipitation provides a very good homogeneity of mechanical properties in the T3W state, which has been observed before but not explained [33]. The subtle differences in cluster radius and volume fraction observed in the different zones of the weld are probably due to complex differences in vacancy concentration at the end of welding due to sweeping by dislocations and high temperature excursion. They will not be discussed in more details because they are not believed to influence significantly the subsequent precipitation kinetics [45].

When the T3W weld is subjected to ageing at 155 °C, we have observed several phenomena that deserve more detailed attention. The two most prominent are the delayed ageing kinetics in the weld nugget and the influence of the height in the nugget on the precipitation and related hardening plateau at long ageing times.

First we will discuss the delayed ageing kinetics. In order to observe more precisely the influence of the location in the weld on the precipitation kinetics, samples for DSC were cut every 3 mm, from the base material to the nugget core, in the T3W state. These samples were then subjected to a DSC scan at 50 K/min, which results are presented in Fig. 11a (only the results for the retreating side are presented for the sake of clarity). The classical DSC behavior for these alloys in a naturally aged state is observed, namely a series of endothermic peaks from 50 °C to 250 °C, followed by a series of exothermic peaks and then the final endothermic peaks before reaching the solution treatment temperature above 500 °C [46]. The low temperature endothermic peaks correspond to the dissolution of the clusters formed during natural ageing and will not be discussed here. The high temperature endothermic peak corresponds to the dissolution of the precipitates formed during heating, and it can be observed that this peak is similar for all conditions, which indicates that between 350 °C and 400 °C all samples reach a similar microstructure. The exothermic peaks correspond to the formation of the precipitating phases. In the base metal (thick blue curve), two well-defined exothermic

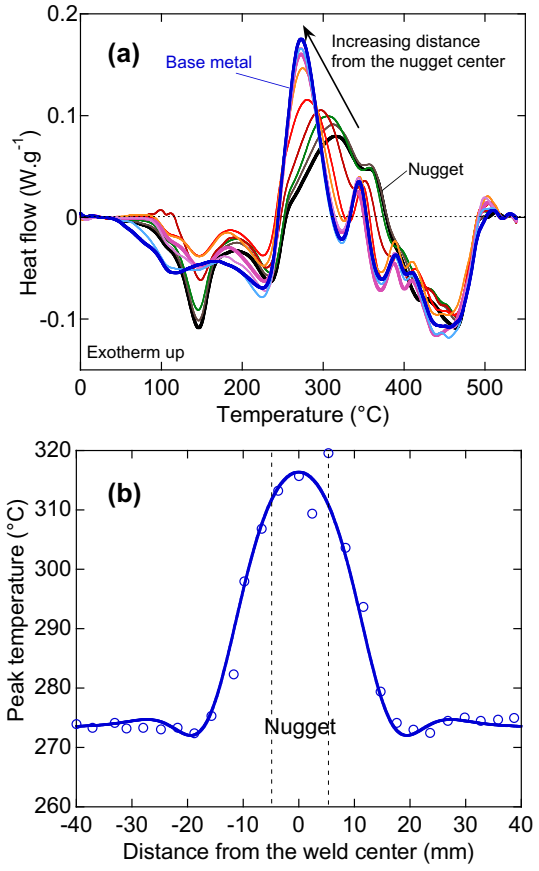

Fig. 11. (a) DSC thermograms realized on samples located every 3 mm from the base material to the weld nugget; (b) evolution of the peak temperature of the main exothermic peak as a function of the position in the weld.

peaks are observed. As shown by a prior study on a similar alloy, these two peaks are characteristic of the formation of T_1 precipitates in a pre-deformed material. The first, main peak represents the formation of T_1 platelets with thickness of one unit cell, and the second, minor peak to the thickening of these T_1 precipitates [46]. When approaching the center of the weld, these two peaks merge into only one, similarly to what has been observed in [23], whose temperature shifts to higher values is better evidenced by Fig. 11b, which shows the main precipitation peak temperature as a function of the position in the weld. This is very consistent with a change in precipitation mechanism resulting in a more sluggish kinetics as one approaches the nugget, and then within this region.

Such delayed kinetics has been observed before, when ageing has been performed on an un-stretched material. Because T_1 nucleates most efficiently on dislocations, their absence provoke a strong delay in precipitation kinetics, and has been observed to favor other types of precipitates such as θ′ [12,45]. Actually, these θ′ precipitates have been observed in the present case to be the majority phase within the nugget. It can actually be expected that the density of dislocations is very low in the nugget and the part of the TMAZ experiencing the highest temperature, because of the recrystallized microstructure (in the nugget) or extensive recovery (in the TMAZ). Even though the internal stresses building up during cooling of the weld may introduce some dislocations in the nugget, it can be expected that their density is much lower than that of the base metal, which has been stretched by 2–4 %. The amount of strain has been shown recently to have a strong influence on the strengthening kinetics in Al–Cu–Li alloys of similar composition to the present 2050 alloy [41], in particular a strong difference

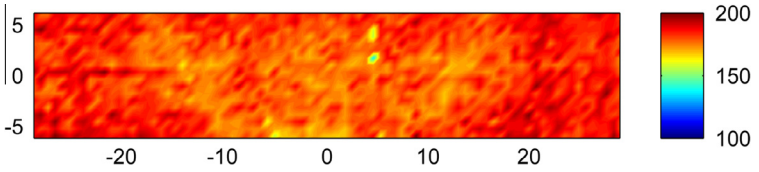

Fig. 12. Microhardness map of the weld cross-section after subjecting a T3W to 10% plastic strain, followed by 30 h of ageing at 155 °C. Color scale is in HV and map scale is in mm.

was observed between a pre-deformation of 0.5 and 2.5%. In order to check the validity of the hypothesis of the lower dislocation density being responsible for the more sluggish precipitation kinetics, two additional experiments were carried out. The first one was to re-solutionize a sample from the base material, and subject it (without prior stretching) to ageing at 155 °C. The resulting hardness evolution, shown in Fig. 9, appears to be similar in kinetics with that of the top line of the nugget, actually much more sluggish than that of the base material, and with a similar plateau value.

According to this hypothesis, it is only the lack of dislocations that prevents the nugget to harden with a similar kinetics as the base material during the post-welding T8 heat treatment. This was verified by subjecting the T3W weld to a general plastic deformation of 10% by rolling (so that the strain is uniformly distributed in the joint), prior to a T8 ageing treatment of 30 h at 155 °C. Subsequently, the distribution of microhardness was mapped in the weld cross-section and is shown in Fig. 12. It appears immediately that the distribution of microhardness in this sample is much more homogeneous as compared to that of the T3WT8 sample (Fig. 7d). At the top of the weld, the hardness is completely homogeneous across the weld and identical to that of the base material. At lower heights within the weld, however, a moderate but significant hardness decrease is still observed, and is most pronounced at the bottom line. These results confirm that adding dislocations to the nugget in the T3W state promotes a much more efficient hardening after T8 heat treatment, and as a consequence this establishes that the main explanation of the sluggish precipitation kinetics of the weld nugget during the artificial ageing leading to the T3WT8 state is the lack of dislocations in this region.

Now the point that remains to be understood is the difference in hardening potential remaining at the bottom of the weld even after introducing a plastic strain. This lack of hardening is actually consistent with the lower hardness plateau observed at long ageing times on the original nugget (see Fig. 9). It is similar, yet smaller in magnitude, to what has been recently observed in an independent study on the same alloy [27].

One likely explanation for the lack of hardening potential in some parts of the nugget is that some of the solute required for hardening is trapped in coarse intermetallic particles, which form during welding or during cooling immediately after the welding operation, at temperatures slightly below the alloy solvus. To test this hypothesis, image analysis was first carried out on FEG-SEM micrographs in backscattered electrons mode, along the three characteristic lines (top, middle and bottom), as a function of the distance from the weld nugget. Most of the observed intermetallics are Cu-rich, often, but not always, associated with Mn or Fe. Their average size is of the order of 100 nm. The measured area fractions are shown in Fig. 13.

From this data it is apparent that the area fraction of intermetallics depends markedly on the position in the nugget. The fraction at the top line is very close to that of the base material, around 0.3–0.4%, corresponding to the coarse equilibrium intermetallic fraction present in the alloy, redistributed as fine particles in the weld nugget by the intense plastic deformation. The middle line approaches a fraction of 0.5% and the bottom line lies between 0.7% and 0.9%. Even though it is difficult to relate this fraction unambiguously to the amount of solute trapped because of some scatter in the composition of the intermetallics, the difference of almost 0.5% is sufficient to explain a difference in strengthening potential between the different zones. This effect was further investigated by subjecting samples from the different welded zones to a new solutionizing treatment at 525 °C, and then to an ageing treatment at 155 °C. Fig. 14 shows that the new solution treatment significantly increases the hardening potential in all the welded zones, thereby confirming that the main cause for the influence of the position in the weld on the hardening potential is the loss of solute to intermetallic particles. This figure also shows a remaining small but significant influence of the position on the plateau hardness. The highest hardness is found in the resolutionized base metal, followed by the top line, then the middle line and last the bottom

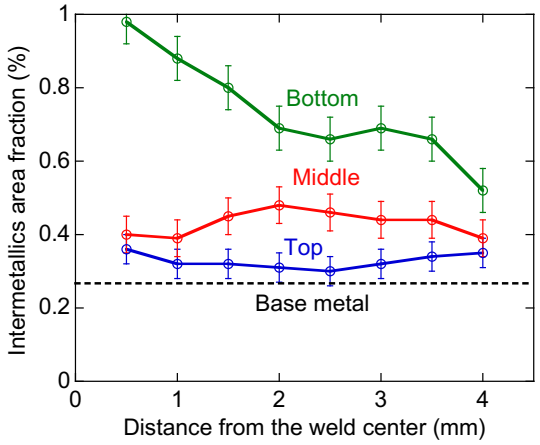

Fig. 13. Distribution of intermetallic area fraction measured by image analysis on SEM micrographs, along the three lines in the weld nugget.

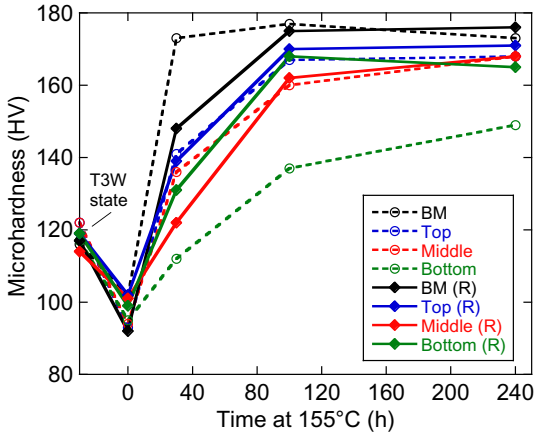

Fig. 14. Microhardness evolution during ageing at 155 °C in the re-solutionized (R) base metal, and nuggets at the top, middle and bottom locations, as compared to the same kinetics realized on the weld.

line. As it is unlikely that any solute is lost during the welding operation because the material stays in the solid state, the cause of this minor effect is probably that some of the supplementary intermetallics have not been dissolved during the post-welding solution treatment.

8. Conclusion

As a result of the systematic approach of mapping the microstructure and hardness in the weld cross-sections after welding and during post-welding treatments of a 2050-T34 friction stir weld, the most prominent phenomena that control the microstructure development in the different zones of the weld can now be summarized:

- In the T3W (as welded and naturally aged) condition, the microstructure is relatively homogenous, and no significant high temperature precipitation is present in any part of the weld. This homogeneity is related to the relatively slow nucleation kinetics of the high temperature phases in this alloy. After welding, clusters form in the different areas of the weld. The two critical temperature ranges are around 200 °C, where clusters initially present dissolve but do not re-form after welding presumably because of a shortage of vacancies, and 250–300 °C where the precipitation of platelet phases is most pronounced during welding.
- The different zones of the weld exhibit very different ageing kinetics when subjected to post-welding heat treatment, due to two main causes. Firstly, a much lower dislocation density in the weld nugget and part of the TMAZ as compared to the initial T34 material, which results in a slow precipitation of θ' instead of a fast precipitation of T_1 in the base material. Secondly, the presence, most pronounced at the bottom of the nugget, of a higher fraction of Cu-containing intermetallic particles formed during welding. These two phenomena have a different signature on the precipitation kinetics in the nugget. The absence of dislocations result in a strengthening delay but has a limited influence on the hardening potential at long ageing times, whereas the fraction of intermetallic particles mostly control this maximum hardness value.
- These differences in hardening kinetics explain the hardness heterogeneity observed after subjecting the T3W state to a post-welding T8 heat treatment. Most of the hardening deficit of the weld nugget can be compensated if a plastic deformation is applied to all weld regions prior to the post-welding heat treatment.

Acknowledgments

This work was financially supported by the ANR Mat&Pro program (ANR-08-MAPR-0020-05 "CORALIS"). The authors would like to thank the staff of the D2AM-BM02 beamline at ESRF. The different partners of the project, and particularly Prof. C. Blanc, are thanked for fruitful discussions. Dr. C. Henon of Constellium C-Tech is additionally thanked for providing the material and Dr. J. Delfosse of Airbus Group Innovations is thanked for providing the welded joint. The authors also thank the students involved in the DSC and hardness measurements (Casey Julich-Trojan and Washington Santos).

References

[1] R.S. Mishra, Z.Y. Ma, Friction stir welding and processing, Mater. Sci. Eng., R 50 (2005) 1–78.
[2] R. Nandan, T. DebRoy, H.K.D.H. Bhadeshia, Recent advances in friction-stir welding – process, weldment structure and properties, Prog. Mater Sci. 53 (2008) 980–1023, http://dx.doi.org/10.1016/j.pmatsci.2008.05.001.
[3] P.L. Threadgill, A.J. Leonard, H.R. Shercliff, P.J. Withers, Friction stir welding of aluminium alloys, Int. Mater. Rev. 54 (2009) 49–93, http://dx.doi.org/10.1179/174328009X411136.
[4] C. Genevois, A. Deschamps, A. Denquin, B. Doisneau cottignies, Quantitative investigation of precipitation and mechanical behaviour for AA2024 friction stir welds, Acta Mater. 53 (2005) 2447–2458.
[5] C. Gallais, A. Simar, D. Fabregue, A. Denquin, G. Lapasset, B. de Meester, et al., Multiscale analysis of the strength and ductility of AA 6056 aluminum friction stir welds, Metall. Mater. Trans. 38A (2007) 964–981, http://dx.doi.org/10.1007/s11661-007-9121-x.
[6] A. Sullivan, J.D. Robson, Microstructural properties of friction stir welded and post-weld heat-treated 7449 aluminium alloy thick plate, Mater. Sci. Eng. 478 (2008) 351–360, http://dx.doi.org/10.1016/j.msea.2007.06.025.
[7] A. Simar, Y. Brechet, B. de Meester, A. Denquin, C. Gallais, T. Pardoen, Integrated modeling of friction stir welding of 6xxx series Al alloys: process, microstructure and properties, Prog. Mater Sci. 57 (2012) 95–183, http://dx.doi.org/10.1016/j.pmatsci.2011.05.003.
[8] T. Warner, Recently-developed aluminium solutions for aerospace applications, Mater. Sci. Forum 519–521 (2006) 1271–1278.
[9] B. Decreus, A. Deschamps, F. De Geuser, P. Donnadieu, C. Sigli, M. Weyland, The influence of Cu/Li ratio on precipitation in Al–Cu–Li–x alloys, Acta Mater. 61 (2013) 2207–2218.
[10] P. Lequeu, K.P. Smith, A. Danielou, Aluminum–copper–lithium alloy 2050 developed for medium to thick plate, J. Mater. Eng. Perform. 19 (2010) 841–847, http://dx.doi.org/10.1007/s11665-009-9554-z.
[11] A. Deschamps, B. Decreus, F. De Geuser, T. Dorin, M. Weyland, The influence of precipitation on plastic deformation of Al–Cu–Li alloys, Acta Mater. 61 (2013) 4010–4021, http://dx.doi.org/10.1016/j.actamat.2013.03.015.
[12] B.M. Gable, A.W. Zhu, A.A. Csontos, E.A.J. Starke, The role of plastic deformation on the competitive microstructural evolution and mechanical properties of a novel Al–Cu–Li–X alloy, J. Light Met. 1 (2001) 1–14.
[13] H.K. Hardy, J.M. Silcock, J. Inst. Met. 84 (1955) 423.
[14] P. Sainfort, B. Dubost, Coprecipitation hardening in Al–Li–Cu-Mg alloys, J. Phys. C3 (9) (1987) 407–413.
[15] S.P. Ringer, B.C. Muddle, I.J. Polmear, Effects of cold work on precipitation in Al–Cu–Mg–(Ag) and Al–Cu–Li–(Mg–Ag) alloys, Metall. Mater. Trans. A 26A (1995) 1659–1671.
[16] R. Yoshimura, T.J. Konno, E. Abe, K. Hiraga, Transmission electron microscopy study of the evolution of precipitates in aged Al–Li–Cu alloys: the θ' and T1 phases, Acta Mater. 51 (2003) 4251–4266.
[17] S.C. Wang, M.J. Starink, Precipitates and intermetallics phases in precipitation hardening Al–Cu–Mg–(Li) based alloys, Int. Mater. Rev. 50 (2005) 193–215.
[18] J.A. Schneider, A.C. Nunes, P.S. Chen, G. Steele, TEM study of the FSW nugget in AA2195-T81, J. Mater. Sci. 40 (2005) 4341–4345, http://dx.doi.org/10.1007/s10853-005-2808-8.
[19] R.W. Fonda, J.F. Bingert, Precipitation and grain refinement in a 2195 Al friction stir weld, Metall. Mater. Trans. 37A (2006) 3593–3604, http://dx.doi.org/10.1007/s11661-006-1054-2.
[20] P. Cavaliere, M. Cabibbo, F. Panella, A. Squillace, 2198 Al–Li plates joined by friction stir welding: mechanical and microstructural behavior, Mater. Des. 30 (2009) 3622–3631, http://dx.doi.org/10.1016/j.matdes.2009.02.021.
[21] A.K. Shukla, W.A.I. Baeslack, Study of microstructural evolution in friction-stir welded thin-sheet Al–Cu–Li alloy using transmission-electron microscopy, Scr. Mater. 56 (2007) 513–516.
[22] A.K. Shukla, W.A. Baeslack, Study of process/structure/property relationships in friction stir welded thin sheet Al–Cu–Li alloy, Sci. Technol. Weld. Join. 14 (2009) 376–387, http://dx.doi.org/10.1179/136217109X412409.
[23] A. Steuwer, M. Dumont, J. Altenkirch, S. Birosca, A. Deschamps, P.B. Prangnell, et al., A combined approach to microstructure mapping of an Al–Li AA2199 friction stir weld, Acta Mater. 59 (2011) 3002–3011, http://dx.doi.org/10.1016/j.actamat.2011.01.040.
[24] F. De Geuser, F. Bley, A. Denquin, A. Deschamps, Mapping the microstructure of a friction-stir welded (FSW) Al–Li–Cu alloy, J. Phys: Conf. Ser. 247 (2010) 12–34, http://dx.doi.org/10.1088/1742-6596/247/1/012034.
[25] R. Ivanov, J. Boselli, D. Denzer, D. Larouche, R. Gauvin, M. Brochu, Hardening potential of an Al–Cu–Li friction stir weld, Proc. 13th Int. Conf. Alum. Alloys Icaa13, 2012, pp. 659–664.
[26] F. De Geuser, B. Malard, A. Deschamps, Microstructure mapping of a friction stir welded AA2050 Al–Li–Cu in the T8 state, Philos. Mag. 94 (2014) 1451–1462, http://dx.doi.org/10.1080/14786435.2014.887862.
[27] M.-N. Avettand-Fenoel, R. Taillard, Heterogeneity of the nugget microstructure in a thick 2050 Al friction-stirred weld, Metall. Mater. Trans. 46A (2015) 300–314, http://dx.doi.org/10.1007/s11661-014-2638-x.
[28] W. Li, R. Jiang, Z. Zhang, Y. Ma, Effect of rotation speed to welding speed ratio on microstructure and mechanical behavior of friction stir welded aluminum–lithium alloy joints, Adv. Eng. Mater. 15 (2013) 1051–1058, http://dx.doi.org/10.1002/adem.201300147.
[29] G. Pouget, A.P. Reynolds, Residual stress and microstructure effects on fatigue crack growth in AA2050 friction stir welds, Int. J. Fatigue 30 (2008) 463–472, http://dx.doi.org/10.1016/j.ijfatigue.2007.04.016.
[30] Y.E. Ma, Z. Zhao, B. Liu, W. Li, Mechanical properties and fatigue crack growth rates in friction stir welded nugget of 2198–T8 Al–Li alloy joints, Mater. Sci. Eng. 569 (2013) 41–47, http://dx.doi.org/10.1016/j.msea.2013.01.044.

[31] T. Le Jolu, T.F. Morgeneyer, A. Denquin, M. Sennour, A. Laurent, J. Besson, et al., Microstructural characterization of internal welding defects and their effect on the tensile behavior of FSW joints of AA2198 Al–Cu–Li alloy, Metall. Mater. Trans. 45A (2014) 5531–5544, http://dx.doi.org/10.1007/s11661-014-2537-1.
[32] T. Le Jolu, T.F. Morgeneyer, A. Denquin, A.F. Gourgues-Lorenzon, Fatigue lifetime and tearing resistance of AA2198 Al–Cu–Li alloy friction stir welds: effect of defects, Int. J. Fatigue 70 (2015) 463–472, http://dx.doi.org/10.1016/j.ijfatigue.2014.07.001.
[33] V. Calogero, G. Costanza, S. Missori, A. Sili, M.E. Tata, A weldability study of Al–Cu–Li 2198 alloy, Metallurgist 57 (2014) 1134–1141, http://dx.doi.org/10.1007/s11015-014-9858-6.
[34] V. Proton, J. Alexis, E. Andrieu, C. Blanc, J. Delfosse, L. Lacroix, et al., Influence of post-welding heat treatment on the corrosion behavior of a 2050–T3 aluminum–copper–lithium alloy friction stir welding joint, J. Electrochem. Soc. 158 (2011) C139–C147, http://dx.doi.org/10.1149/1.3562206.
[35] V. Proton, J. Alexis, E. Andrieu, J. Delfosse, A. Deschamps, F. De Geuser, et al., The influence of artificial ageing on the corrosion behaviour of a 2050 aluminium–copper–lithium alloy, Corros. Sci. 80 (2014) 494–502, http://dx.doi.org/10.1016/j.corsci.2013.11.060.
[36] M. Dhondt, I. Aubert, N. Saintier, J.M. Olive, Effects of microstructure and local mechanical fields on intergranular stress corrosion cracking of a friction stir welded aluminum–copper–lithium 2050 nugget, Corros. Sci. 86 (2014) 123–130, http://dx.doi.org/10.1016/j.corsci.2014.05.001.
[37] M. Dumont, A. Steuwer, A. Deschamps, M. Peel, P.J. Withers, Microstructure mapping in friction stir welds of 7449 aluminium alloy using SAXS, Acta Mater. 54 (2006) 4793–4801.
[38] O. Glatter, O. Kratky, Small Angle X-Ray Scattering, Academic Press, London, 1982.
[39] J. Epperson, B. Loomis, J. Lin, Quantitative comparison of the void distribution in a Beta'-phase Ni–Al-in alloy using X-ray small-angle scattering and transmission electron-microscopy, J. Nucl. Mater. 108 (1982) 476–484, http://dx.doi.org/10.1016/0022-3115(82)90519-0.
[40] B. Malard, B. Remy, C. Scott, A. Deschamps, J. Chene, T. Dieudonne, et al., Hydrogen trapping by VC precipitates and structural defects in a high strength Fe–Mn–C steel studied by small-angle neutron scattering, Mater. Sci. Eng. 536 (2012) 110–116, http://dx.doi.org/10.1016/j.msea.2011.12.080.
[41] T. Dorin, A. Deschamps, F. De Geuser, C. Sigli, Quantification and modelling of the microstructure/strength relationship by tailoring the morphological parameters of the T1 phase in an Al–Cu–Li alloy, Acta Mater. 75 (2014) 134–146, http://dx.doi.org/10.1016/j.actamat.2014.04.046.
[42] A. Deschamps, F. De Geuser, Quantitative characterization of precipitate microstructures in metallic alloys using small-angle scattering, Metall. Mater. Trans. 44A (2013) 77–86, http://dx.doi.org/10.1007/s11661-012-1435-7.
[43] W.A. Cassada, G.J. Shiflet, E.A.J. Starke, The effect of plastic deformation on Al2CuLi (T1) precipitation, Metall. Trans. A 22A (1991) 299–306.
[44] F. De Geuser, F. Bley, A. Deschamps, A new method for evaluating the size of plate-like precipitates by small-angle scattering, J. Appl. Crystallogr. 45 (2012) 1208–1218, http://dx.doi.org/10.1107/S0021889812039891.
[45] B. Decreus, A. Deschamps, F. de Geuser, C. Sigli, Influence of natural ageing and deformation on precipitation in an Al–Cu–Li alloy, Adv. Eng. Mater. 15 (2013) 1082–1085, http://dx.doi.org/10.1002/adem.201300098.
[46] T. Dorin, A. Deschamps, F. De Geuser, W. Lefebvre, C. Sigli, Quantitative description of the T1 formation kinetics in an Al–Cu–Li alloy using differential scanning calorimetry, small-angle X-ray scattering and transmission electron microscopy, Philos. Mag. 94 (2014) 1012–1030, http://dx.doi.org/10.1080/14786435.2013.878047.